

# **Imaging Intravoxel Vessel Size Distribution in the Brain Using Susceptibility Contrast Enhanced MRI**

## **Author Information**

---

### Affiliations

**Department of Cancer Systems Imaging, Cancer Neuroscience Program, Neuroimaging Innovations to Transform Cancer Care (NeuroCare) Program, The University of Texas MD Anderson Cancer Center, Houston, TX, 77025, USA**

Natanael B. Semmineh, Indranil Guha, Deborah Healey, Anagha Chandrasekharan, C. Chad Quarles

**Department of Diagnostic Imaging, Rhode Island Hospital, Providence, RI, 02903, USA**

Jerrold L. Boxerman

**These authors contributed equally:** Natanael B. Semmineh, Indranil Guha

### Contributions

N.B.S., I.G. ‘Conceptualized the project, developed the MR signal simulation tool, image analysis algorithms, and deep learning model, designed the experiments, analyzed the data, and wrote the manuscript.’, D.H. and A.C. ‘Acquired the LSFM images and wrote the manuscript’, J.L.B. ‘Conceptualized the project, analyzed the data, and wrote/edited the manuscript.’, C.C.Q. ‘Conceptualized, supervised, and acquired funds for the project, and developed the methodology, designed experiments, analyzed data, and wrote/edited the manuscript’. All the authors discussed the results and commented on the manuscript. All authors have approved the final version of the manuscript.

### Corresponding author

C. Chad Quarles, Cancer Systems Imaging, 1881 East Road, Unit 1907, Houston, TX 77054-1907, USA,  
Phone: (+1) 832-885-8540, Email: [ccquarles@mdanderson.org](mailto:ccquarles@mdanderson.org).

## **Abstract**

---

Vascular remodelling is inherent to the pathogenesis of many diseases including cancer, neurodegeneration, fibrosis, hypertension, and diabetes. In this paper, a new susceptibility-contrast based MRI approach is established to non-invasively image intravoxel vessel size distribution (VSD), enabling a more comprehensive and quantitative assessment of vascular remodelling. The approach utilizes high-resolution light-sheet fluorescence microscopy images of rodent brain vasculature, simulating gradient echo sampling of free induction decay and spin echo (GESFIDE) MRI signals for the three-dimensional vascular networks, and training a deep learning model to predict cerebral blood volume (CBV) and VSD from GESFIDE signals. The results from *ex vivo* experiments demonstrated strong correlation ( $r = 0.96$ ) between the true and predicted CBV. High similarity between true and predicted VSDs was observed (mean Bhattacharya Coefficient = 0.92). With further *in vivo* validation, intravoxel VSD imaging could become a transformative preclinical and clinical tool for interrogating disease and treatment induced vascular remodelling.

## **Introduction**

---

Vessel size distribution (VSD) is a fundamental feature of vascular architecture, tightly linked to physiological function, metabolism, and pathological processes. In healthy tissues, vascular organization is finely regulated to meet organ-specific metabolic demands, ensuring efficient blood flow and oxygen delivery. In disease, this balance is disrupted and aberrations in vascular architecture become defining features of many pathological conditions. For example, tumor angiogenesis leads to disordered vascular morphology and networks,<sup>1-4</sup> while luminal narrowing and capillary rarefaction restrict blood flow in atherosclerosis.<sup>5</sup> Microvascular changes in liver fibrosis include increased tortuosity, abnormal branching patterns, and reduced vascular density. Diabetic microangiopathy is characterized by injury to arterioles and venules along with pro- and anti-neovascularization, leading to premature blood vessels and micro-

thrombosis.<sup>6,7</sup> Cerebral small-vessel disease (CSVD), a major contributor to stroke and dementia is marked by capillary rarefaction, vessel narrowing, and autoregulatory dysfunction, leading to chronic hypoxia, impaired cerebral blood flow, and cognitive decline.<sup>8,9</sup> Microvascular damage in Alzheimer's disease impairs cerebral blood flow, promotes amyloid-beta accumulation, and contributes to cognitive decline,<sup>10,11</sup> whereas in Parkinson's disease, vessel remodelling and reduced blood flow lead to neuronal damage.<sup>12,13</sup> Given the widespread impact of vascular abnormalities across multiple organ systems, the non-invasive determination of intravoxel vessel size heterogeneity could be a transformative tool for tissue and disease characterization, mechanistic explorations, diagnostics, and treatment response assessment in both animals and humans.

Accurately and non-invasively imaging VSD remains an unmet challenge, with current efforts relying on *ex vivo* microscopy, which though informative, is limited by sampling constraints and unsuitability for *in vivo* or longitudinal studies. MRI enables non-invasive and multi-organ imaging, while contrast agent (CA) enhancement further allows for the assessment of tissue structure and function through pre- and post-injection MR imaging. After CA administration, the decrease in longitudinal ( $T_1$ ) and transverse ( $T_2$  and  $T_2^*$ ) relaxation times of tissue water is, in part, determined by the CA concentration. Regarding CA-induced  $T_2$  and  $T_2^*$  changes, when CA is introduced into blood vessels, it creates a susceptibility difference between the vessels and the surrounding tissue. The susceptibility difference generates magnetic field inhomogeneities surrounding the blood vessels (and whose magnitude depends on the vascular architecture) leading to enhanced proton dephasing in the extravascular space and a decrease in the transverse relaxation times.

The most common technique relying on  $T_2$  and  $T_2^*$  changes, dynamic susceptibility contrast (DSC)-MRI, employs gradient-echo (GE) or spin-echo (SE) acquisitions to measure changes in transverse relaxation rates ( $\Delta R_2^*$  and  $\Delta R_2$ ), enabling the computation of perfusion parameters.<sup>14</sup> When a simultaneous GE and SE sequence is utilized, measures of mean vessel size within a voxel can be derived, an approach termed as vessel size imaging.<sup>15</sup> Biophysically, vessel size imaging relies upon the differential vessel size sensitivity of GE and SE signal.<sup>16-20</sup> Simulations and experimental data have shown that the change in the

GE relaxation rate ( $\Delta R_2^*$ ) initially increases for very small perturber sizes and then plateaus as perturber size increases. In contrast, the SE relaxation rate change ( $\Delta R_2$ ) increases, peaks, and then decreases with a maximal sensitivity towards capillary sized perturbers.<sup>21</sup> The ratio of  $\Delta R_2^*$  and  $\Delta R_2$  was first used as a relative measure of mean vessel diameter,<sup>22</sup> while the Q-index ( $Q = \Delta R_2 / \Delta R_2^{*2/3}$ ) was later introduced as a measure of microvascular density.<sup>23</sup> Analytical models for mean vessel radius and vessel size index (VSI) rely on the ratio of  $\Delta R_2^*$  and  $\Delta R_2$ , the apparent diffusion coefficient, and the susceptibility difference ( $\Delta \chi$ ), assuming a static dephasing regime.<sup>15,24</sup> However, these models often overestimate vessel size due to high  $\Delta \chi$  assumptions and simplified representations of vessel shape and water diffusion.<sup>24</sup>

A more sophisticated approach for quantifying mean vessel size, blood volume, and oxygenation, termed MR vascular fingerprinting (MRvF), was proposed to overcome prior assumptions and enable higher resolution vessel size imaging.<sup>25-28</sup> Christensen *et al.*<sup>26</sup> pioneered the MRvF technique where they created a dictionary of simulated GE sampling of the free induction decay and spin echo (GESFIDE) signal pre- and post-injection of an iron-based CA using virtual voxels containing two-dimensional (2D) blood vessels with varying cerebral blood volume (CBV), mean vessel radius, and blood oxygenation saturation ( $SO_2$ ). The dictionary was used to predict aforementioned vascular parameters for any given MRI signal and the experimental results on the healthy human brain showed that the parametric maps predicted from the MRvF was consistent with the same maps obtained from the conventional MR methods. Boux *et al.*<sup>25</sup> proposed a novel dictionary-based statistical learning method to estimate vascular parameters from MRvF with higher accuracy at lower computational cost. Pouliot *et al.*<sup>28</sup> used realistic cortex angiograms of mouse instead of synthetic vessel models for MRvF to better capture vascular complexity. They found that parameter estimates were biased when different angiograms were used for dictionary matching, but their method improved physiological accuracy over 2D models. This approach revealed significantly lower  $SO_2$ , CBV, and mean vessel radius in atherosclerotic mice compared to the wild type mice. Recently, Delphin *et al.*<sup>27</sup> extended the original MRvF technique using three-dimensional (3D) vascular structures extracted from microscopic images of whole mouse brain vasculature and showed that the mean radius, blood volume

fraction (bvf), and  $\text{SO}_2$  estimates obtained using their approach have better agreement with the literature than same measures obtained using 2D or 3D cylindrical models. However, the paper does not report any quantitative metric demonstrating the agreement between the true and predicted parameters.

The advantage of GESFIDE lies in its sensitivity to a broader spectrum of microstructural variations by integrating GE, asymmetric spin echo (ASE), and SE contrasts. With respect to the vasculature, GE is sensitive to vessels of all sizes, SE is primarily sensitive to capillary sized vessels, and ASE provides an intermediate sensitivity. GESFIDE effectively combines these contributions into a more comprehensive vascular fingerprint. However, despite the enhanced sensitivity of GESFIDE, both VSI and MRvF provide mean vascular parameters within a MR voxel that does not reflect the underlying heterogeneity of the vascular architecture. For example, two volumes of interest (VOIs) (Fig. 1(a,b)) extracted from light-sheet fluorescence microscopy (LSFM) images of a cleared whole mouse brain vasculature with similar mean radius (VOI1:  $5.56 \mu\text{m}$ , VOI2:  $5.82 \mu\text{m}$ ) and CBV (VOI1: 4.40%, VOI2: 4.51%) exhibited distinct VSDs (Fig. 1(c)). The VOI1 had a larger area under the curve than the VOI2. This highlights that while mean vascular parameters provide a useful summary, VSD offers deeper insight into the underlying heterogeneity of the vascular network by better capturing its influence on MR signal variability.

In this paper, we present a deep learning (DL) approach that expands upon the MRvF framework by replacing traditional dictionary matching with a data-driven model that leverages realistic vascular networks from rodent whole-brain LSFM images. This approach moves beyond conventional mean vessel size estimation by enabling voxel-wise evaluation of VSD. LSFM was used to image the whole-brain vasculature of rodents, followed by a custom-developed image processing pipeline for binary segmentation of vascular structures and computation of true CBV and VSD. Small (voxel-sized) VOIs containing segmented blood vessels were then extracted to simulate GESFIDE signals before and after the injection of the iron-based contrast agent, ferumoxytol. Building upon the dictionary matching approach of MRvF, we trained a fully connected neural network (FCN) for more robust prediction of CBV and VSD from the ratio of pre- and post-contrast GESFIDE signals. The performance of the DL model was evaluated by comparing

predicted VSD with ground truth measurements, and the accuracy of the mean vessel radius computed from the predicted VSD was assessed against analytically derived values. Additionally, the model was validated using a publicly available dataset of segmented mouse brain vasculature,<sup>29</sup> further demonstrating its ability to generalize across realistic vascular networks.

## Results

---

The mean $\pm$  standard deviation (SD) of the true and predicted CBV values for the test VOIs was  $14.71\pm 6.52$  and  $15.59\pm 6.67\%$ , respectively with a mean relative error (MRE) of 9%. The scatter plot of true and predicted CBV values (n=2,158) are shown in Fig. 2(a). A strong linear correlation ( $r = 0.96$ ) can be observed between the two sets of values with the trend-line closely following the identity line with a slope and intercept of 0.99 and 0.96, respectively. The Bland-Altman plot of the difference between true and predicted CBV values are shown in 2(b). The mean difference between the true and predicted CBV was 0.87% and 97% of the residuals were within  $\pm 1.96SD$ , i.e.  $\pm 3.75\%$ , of the mean difference. Fig. 3 shows the color-coded true (3(a)) and predicted (3(b)) CBV maps over an entire axial slice of the mouse brain. Visual similarity between the true and predicted CBV maps can be observed which is further supported by the difference image in 3(c), where most of the pixels are white demonstrating a very low difference between the true and predicted CBV values. The mean absolute difference (MAD) between the true and predicted CBV maps was 2.11%.

The qualitative results of VSD prediction for 12 VOIs with CBV varying from 2.5 to 24% are shown in Fig. 4. Significant overlap between the true (green) and predicted (red) VSDs can be observed for all 12 VOIs. The Bhattacharyya coefficient (BC) values for the test VOIs (n=2,158) are plotted against their true mean radius in Fig. 5(a). The mean $\pm$ SD of the BC values were  $0.92\pm 0.08$  and 69% of the VOIs showed a BC of  $\geq 0.92$  while the BC for 90% of the VOIs were within  $\pm 1SD$  of the mean value. The mean $\pm$ SD of the coefficient of variation (CV) for the true and predicted VSDs were  $47.87\pm 13.81$  and  $54.25\pm 15.60\%$ , respectively. The mean $\pm$ SD of the true and predicted mean radius were  $6.91\pm 2.01$  and  $6.82\pm 1.43 \mu\text{m}$ , respectively with 14% MRE between them. The Bland-Altman plot of the true and predicted

mean radius (5(b)) shows a mean difference of 1.49  $\mu\text{m}$  with 95% of the residuals falling within  $\pm 1.96\text{SD}$ , i.e.  $\pm 2.83 \mu\text{m}$ , of the mean difference. The VSI for each VOI was computed using the Equation (1) where the values of  $ADC$ ,  $\gamma$ ,  $B_0$ , and  $\Delta\chi$  were set to  $1 \mu\text{m}^2/\text{ms}$ ,  $4.258 \times 10^7 \text{ s}^{-1}\text{T}^{-1}$ , 3 T, and  $10^{-6}$ , respectively. The mean $\pm$ SD of the VSI was  $6.94\pm 3.94 \mu\text{m}$  and 58% MRE was observed between the true mean radius and VSI. The Bland-Altman plot of (5(c)) shows a mean difference of 1.62  $\mu\text{m}$  between the true mean radius and VSI with 95% of the residuals falling within  $\pm 1.96\text{SD}$ , i.e.  $\pm 7.73 \mu\text{m}$ , of the mean difference.

The color-coded CV and BC maps derived from the true and predicted VSDs over an entire axial slice of mouse brain is shown in Fig. 6. The true (6(a)) and predicted (6(b)) CV maps show good visual similarity which is further supported by a mostly white difference image (6(c)). The MAD between the two CV maps was 3.35%. The BC map (6(d)) has mostly red pixels ( $BC > 0.80$ ) that further demonstrates high similarity between the true and predicted VSDs. The mean BC over the entire axial slice was 0.89. Fig. 7 shows the color-coded maps of true and predicted mean radius and VSI. Visually, the true mean radius values (7(a)) are lower than both the predicted mean radius (7(b)) and VSI values (7(c)). The difference map of the true and predicted mean radius (7(d)) has higher number of white pixels than the difference map (7(e)) of the true mean radius and VSI, which demonstrates that the predicted radius are closer to the true value than the VSI. The MAD between the true and predicted mean radius was 0.42  $\mu\text{m}$ , whereas, the MAD between the true mean radius and VSI was 7.77  $\mu\text{m}$ .

The mean $\pm$ SD of the true and predicted CBV values ( $n=1,000$ ) for the publicly available dataset were  $6.76\pm 4.29$  and  $6.75\pm 4.23\%$ , respectively with a MRE of 10%. The linear correlation of 0.98 was observed between the true and predicted CBV. The trend-line closely followed the identity line with a slope and intercept of 0.97 and 0.42, respectively. The mean $\pm$ SD of the BC values were  $0.89\pm 0.08$  and 60% of the VOIs showed a BC of  $\geq 0.89$  while the BC for 91% of the VOIs were within  $\pm 1\text{SD}$  of the mean value. The mean $\pm$ SD of the CV for the true and predicted VSDs were  $37.62\pm 7.04$  and  $46.27\pm 13.04\%$ , respectively. The mean $\pm$ SD of the true and predicted mean radius were  $5.27\pm 1.21$  and  $5.67\pm 1.11 \mu\text{m}$ ,

respectively with 16% MRE between them. The mean $\pm$ SD of the VSI was 11.40 $\pm$ 5.35  $\mu$ m while the MRE with the true mean radius was 117%.

## Discussion

---

The results of this study provide strong evidence that imaging intravoxel VSD is feasible using pre- and post-contrast GESFIDE MRI data and the established DL network. A significant feature of the approach is that it intrinsically decouples the complex relationship between voxel-wise, CA concentration, heterogeneous vascular architecture, and the measured changes in transverse relaxation rates. With traditional DSC-MRI, this relationship, which varies across voxels, is unknown and prevents absolute quantation of the derived hemodynamic parameters. Practically, the *in vivo* data needed to image VSD is equivalent to MRvF; steady-state GESFIDE data collected prior to and after the injection of an iron-oxide based intravascular CA.

Several histopathological studies<sup>30-32</sup> have previously reported weak to moderate linear correlations ( $r \in [0.42 \text{ } 0.74]$ ) between the MRI-derived relative CBV measure and histology-derived fractional CBV and vessel density measures. High linear correlation ( $r=0.96$ ) and low MRE (9%) between the true and predicted CBV observed in our study demonstrates that integrating 3D realistic vascular structures with MRvF enable accurate quantification of the true CBV, unlike the relative measures derived from DSC-MRI.<sup>33</sup> Christensen *et al.*<sup>26</sup> and Boux *et al.*<sup>25</sup> evaluated the accuracy of CBV prediction from MRvF using virtual VOIs containing 2D cylindrical vessels of uniform radius. Both studies found relatively lower error (MRE  $\sim$  4%) between the true and predicted CBV than ours but also reported higher error for higher CBV values. Low mean difference and absence of residual trend in the Bland-Altman plot of Fig. 2(b) demonstrates that our DL model is free of any systemic bias towards the higher CBV.

High BC values and low difference in mean CV between the true and predicted VSDs demonstrate that the DL model is sensitive to the subtle variations in GESFIDE signal caused by the underlying vascular structure in a VOI and accurately predicts VSD from the signal. The mean vessel radius computed from the predicted VSD was closer to the true mean radius compared to VSI. However, the error between the true

and predicted mean radius (MRE = 14%) was higher than the error between the true and predicted mean radius (MRE = 9%) reported by Christensen *et al.*<sup>26</sup> The relatively higher error observed between the true and predicted CBV and mean radius in our study may be attributed to the intrinsic shortcoming of a DL model in differentiating GESFIDE signals simulated from sophisticated realistic structures with higher degrees of freedom (e.g. non-uniform vessel radius, and shape heterogeneity) than simplistic 2D cylindrical structures. The Bland-Altman plots in Fig. 5 show that the VSI overestimates the true mean radius and the variability of the residuals between true mean radius and VSI are ~3 times higher than the variability of the residuals between true and predicted mean radius. This result is consistent with histological studies<sup>31,34,35</sup> reporting overestimation of vessel sizes by MRI-derived VSI measure. The lesser agreement of the VSI values with the true mean radius may be due to the following assumptions made to derive Equation (1) — (i) the vessels are infinitely long cylinders of uniform radius, (ii) static dephasing,<sup>36</sup> and (iii) slow-diffusion approximation<sup>24</sup> for estimating  $\Delta R_2^*$  and  $\Delta R_2$ , respectively. In contrary, the predicted VSD and mean vessel radius are free from any assumptions of vessel shape, size, and diffusion approximations. Hence, VSD not only allows the computation of mean vessel radius but also provides a tool to accurately quantify the contribution of different vessel sizes to the mean vessel radius measure. The quantitative evaluative results on the publicly available dataset were comparable to those observed in our test dataset. These observations demonstrate that the GESFIDE simulation and VSD computation algorithms, and trained DL models are not biased towards the tissue clearing process, LSFM imaging parameters, and vessel segmentation algorithm, rendering them readily applicable across different datasets without retraining the DL models.

There are few limitations of the current study that should be clarified. First, due to the high-noise and the resolution limitation of the LSFM image, very small (<1.8  $\mu\text{m}$ ) capillaries may merge together and result in erroneous computation of skeletal points and vessel radius. As the computation of the true VSD is sensitive to both the localization error in the skeletal points and the over or under segmentation of the vascular structures, the DL model will have intrinsic learning error that can only be fixed by using more accurately segmented vascular structure. However, developing a highly accurate vessel segmentation

algorithm is beyond the scope of the current paper. Second, the DL model was validated using whole brain LSFM images of a healthy rat and a mouse, hence an extensive validation of the proposed DL method on diseased animal models is imperative. Third, the maximum vessel radius observed in 22,000 VOIs used for training and validation of the DL model was 20  $\mu\text{m}$ . So, the model needs to be validated on vascular structures with radius higher than 20  $\mu\text{m}$ , specifically for translating the method into human brain where the vessel radius reaches up to 3 mm. Fourth, the simulated GESFIDE signals are free from physiological and thermal noise which are common for *in vivo* MRI scans. Hence, the performance of the DL models on GESFIDE signals degenerated by different level of noise needs to be investigated before validating these models on *in vivo* MRI scans. Fifth, the significant heterogeneity in vascular morphology such as vessel radius, length, and density among different organs may require the development of organ specific DL models for accurate VSD prediction. Finally, future studies will explore whether the developed algorithms can be applied, at least to some degree, to DSC-MRI scans acquired with clinical Gadolinium-based contrast agents and spin and gradient echo (SAGE) type pulse sequences. The SAGE pulse sequence is an echo planar version of GESFIDE and provides a reduced number of gradient echos, asymmetric spin echos, and spin echos.

In summary, this is the first study to develop and validate a prediction model for estimating VSD from pre- and post-contrast GESFIDE signals simulated from 3D vascular structures extracted from the LSFM images of whole rodent brains. Although extensive *in vivo* validation of the DL model is required, the findings of our *ex vivo* experiments have shown the potential of VSD imaging as a new imaging approach to quantitatively characterize vascular remodelling associated with disease and therapy.

## Methods

---

In this section, we describe the methods and experimental plans to train and test the DL network for predicting VSD from GESFIDE signal simulated from realistic vascular structures. Towards this goal, following materials and methods were used — (1) animal preparation and LSFM imaging, (2) vasculature

segmentation and VSD computation, (3) GESFIDE signal simulation, (4) VSD prediction using DL, and (5) experiments and data analysis.

## Animal Preparation and LSFM Imaging

LSFM images of a rat and a mouse brain were used to train and test the DL models. Fig. 8 shows the steps involved in animal preparation and LSFM imaging of the rodent brains. First, the animals were sacrificed via trans-cardiac perfusion following the protocol published by Scarpelli *et al.*<sup>37</sup> Just before perfusion, the blood vessel walls in the brain were highlighted by intravenously administering 100  $\mu\text{L}$  (mouse) or 500  $\mu\text{L}$  (rat) of fluorescently labelled lectin antibody (DyLight 649-labelled Lycopersicon Esculentum Lectin, Vector Laboratories, Burlingame, California). After sacrificing the animal, the brain was removed from the skull (8(a)). Paraformaldehyde-fixed samples then underwent an additional preservation step using SHIELD reagents (LifeCanvas Technologies) as per the manufacturer's instructions.<sup>38</sup> Samples were delipidated using LifeCanvas Technologies Clear+ dilapidation reagents and incubated in 50% EasyIndex (RI = 1.52, LifeCanvas Technologies) overnight at 37 °C followed by 1 day incubation in 100% EasyIndex for refractive index matching. The whole-brain vasculature of the rat and mouse were scanned on 3i AxL cleared tissue LSFM scanner (Intelligent Imaging Innovations, Inc., Denver, CO, USA) and SmartSPIM LSFM scanner (Life Canvas Technologies, Cambridge, MA, USA), respectively. Samples imaged on the 3i microscope were imaged in the refractive index matching solution. Samples imaged on the SmartSpim microscope were mounted in 2% ultra-low melt agarose made with EasyIndex, reincubated overnight in EasyIndex, and submerged in EasyIndex matched immersion oil (LifeCanvas Technologies) for imaging (8(b)). The rat brain was acquired at an anisotropic resolution of  $1 \times 1 \times 3 \mu\text{m}$ , whereas the mouse brain was scanned at an isotropic resolution of  $1.8 \mu\text{m}$ . A 3D rendition of the whole rat brain vasculature is shown in (8(c)) and a small VOI is zoomed in for better representation of the highlighted vascular structures. Note that, lectin only stains the vessel wall which makes the lumen of large vessels appear as cavities in the LSFM images while the small vessels appear to be filled. All animal

experiments were conducted after the approval from the Institutional Animal Care and Use Committee (IACUC) at Barrow Neurological Research Institute.

## Vasculature Segmentation and VSD Computation

Rat LSFM images were first resampled at isotropic resolution of  $1.8 \mu\text{m}$  using linear interpolation. Next, 11,000 VOIs with an array size of  $123 \times 123 \times 123$  were randomly sampled from each of the two (1 rat and 1 mouse) LSFM images, resulting in total 22,000 VOIs. Each VOI was passed through an image processing cascade for binary segmentation of the vascular structures and computation of VSD. The image processing cascade was comprised of the following sequential steps — (1) first, contrast limited adaptive histogram equalization (CLAHE) was applied to enhance the contrast of the vascular structures. (2) After contrast enhancement, the vasculature was segmented using the binary thresholding algorithm by Li *et al.*<sup>39</sup> (3) Next, 3D morphological dilation followed by erosion was applied on the segmented structures to fill the hollow lumen of the segmented large vessels and the maximally connected vascular network was extracted. A spherical kernel with  $1 \mu\text{m}$  radius was used for dilation and erosion, and the true CBV was computed as the ratio of non-zero voxels to the total number of voxels in the segmented structure. (4) The skeleton of the segmented vascular structure was extracted using the algorithm by Lee *et al.*<sup>40</sup> Next, each skeletal branch, representing individual vessels, was uniquely labelled using in-house python code. (5) The radius at each skeletal point was computed using the method by Liu *et al.*<sup>41</sup> and the radius of a vessel was determined as the average of the radius values computed at all skeletal points corresponding to that vessel. The mean radius of a VOI was computed as the average radius of all the vessels. (6) The histogram of the vessel radius values with a bin size of  $1 \mu\text{m}$  was computed and normalized by dividing with the maximum vessel count to derive the true VSD of a VOI. Specifically, the height of the  $i^{\text{th}}$  bin in the VSD represents the normalized count ( $c_i \in [0 1]$ ) of vessels with radius  $i \mu\text{m}$ . Fig. 9 illustrates the image processing cascade for vasculature segmentation and VSD computation.

## GESFIDE Signal Simulation

To model the GESFIDE signal evolution, we employed our Finite Perturber Finite Difference Method (FPFDM), a validated computational tool developed by our group, to simulate MR signal changes in realistic 3D tissue structures.<sup>42,43</sup> The vascular structures derived from LSFM served as the input to the FPDF method, ensuring accurate representation of *in vivo* vascular architecture. VSD imaging is performed using ferumoxytol, an intravascular iron oxide based contrast agent. Additional input parameters include static field strength ( $B_0=3$  T), susceptibility difference ( $\Delta\chi=1$  ppm), water diffusion coefficient ( $D=10^{-3}$  mm<sup>2</sup>/s). Using these inputs, a GESFIDE dataset with 18 echo times (10–180 ms) was generated, producing a comprehensive set of signals that serve as input for DL based inference of VSD and CBV. All simulations are conducted using our in-house MATLAB (MathWorks, Natick, MA) code. VSD and simulated GESFIDE signals from VOIs containing vascular structures with varying CBV are shown in Fig. 10.

## VSD Prediction using DL

A two-stage DL network was trained to predict the VSD from the ratio of the simulated pre- and post-contrast GESFIDE signals. The proposed DL network is shown in Fig. 11(a). The network is a combination of two FCNs, where the first network, denoted as the CBV estimator (CBVE), predicts the CBV of a VOI from the ratio of the pre- and post-contrast GESFIDE signals and passes it to the second network called the VSD estimator (VSDE). The VSDE takes both the GESFIDE signal and the predicted CBV as input to estimate the VSD. The network is trained in two-steps — first, the CBVE is trained with the objective of minimizing the mean squared error (MSE) between the true and predicted CBV. Next, the weights of the CBVE are set to non-trainable and the VSDE is trained to predict the VSD by minimizing the MSE between the true and predicted VSD.

The CBVE (Fig. 11(b)) is consisted of 1 input layer, 8 hidden layers ( $h_i$ ), and 1 output layer. The input layer has 18 nodes corresponding to the GESFIDE signal values ( $s_i$   $i=[10\ 180]$  ms) at 18 echo times spaced at an interval of 10 ms. The 8 hidden layers consist of 2048, 1024, 512, 256, 128, 64, 16, and 8 nodes, whereas the output layer has only one node corresponding to the predicted CBV (CBV'). The ReLU<sup>44</sup> activation function was applied at all hidden layers and the output layer. The VSDE (Fig. 11(c)) is

a combination of 1 input layer, 6 hidden layers, and 1 output layer. The input layer has 19 nodes corresponding to 18 echo times of the GESFIDE signal and the CBV'. The 6 hidden layers have 2048, 1024, 512, 256, 128, and 64 nodes with ReLU activation. The output layer is consisted of 40 nodes where node  $i$  corresponds to the predicted normalized count ( $c_i'$ ) of vessels with radius  $i$   $\mu\text{m}$ . A sigmoid<sup>45</sup> activation function was applied at the output layer to restrict the values of the output nodes between 0 and 1.

The set of 22,000 VOIs were split into training, validation, and test dataset in 8:1:1 ratio after removing 420 VOIs with CBV lower than 1% and higher than 25% as they were sampled from the noisy background region and did not include any vascular structures. Hence, the total number of VOIs in the training, validation, and test set were 17,264, 2,158, and 2,158, respectively. For training, the weights of the two FCNs were initialized following the techniques proposed by He *et al.*<sup>46</sup> Each network was trained using Adam optimizer<sup>47</sup> with  $\beta_1 = 0.5$  and  $\beta_2 = 0.9$  and learning rate of  $10^{-4}$  until the training and validation losses converge.

## Experiments and Data Analysis

The performance of the CBVE and VSDE were evaluated on the test dataset. The mean  $\pm$  SD of the true and predicted CBV were computed and the Pearson correlation ( $r$ ) between the two sets of CBV values across all the test VOIs ( $n=2,158$ ) was measured. The MRE (%) between the true and predicted CBV values was computed and the agreement between the true and predicted CBV values was examined using the Bland-Altman plot.

The accuracy of the predicted VSD was evaluated using BC which measures the similarity between the true and predicted VSDs and the mean  $\pm$  SD of the BC values are reported. The CV of the true and predicted VSDs was computed for each VOI and their mean  $\pm$  SD are reported. For each VOI, the predicted mean vessel radius was computed from the predicted VSD as the weighted average of the radius values. The mean  $\pm$  SD of the true and predicted mean radius as well as the MRE between them were calculated.

The agreements of the true mean radius with the predicted mean radius and the steady-state estimate of the VSI were evaluated using Bland-Altman plots. The VSI was derived using the equation by Tropr es *et al.*<sup>15</sup>

$$\text{VSI} = 0.425 \left( \frac{ADC}{\gamma \Delta \chi B_o} \right)^{\frac{1}{2}} \left( \frac{\Delta R_2^*}{\Delta R_2} \right)^{\frac{3}{2}}, \quad (1),$$

where  $ADC$  is the diffusion coefficient,  $\gamma$  is the gyromagnetic constant,  $\Delta \chi$  is the susceptibility difference due to the presence of CA,  $B_o$  is the external magnetic field, and  $\Delta R_2^*$  and  $\Delta R_2$  are the changes in transverse relaxation rates induced by CA. The analytical equations proposed by Stokes *et al.*<sup>48</sup> were used to compute  $\Delta R_2^*$  from the pre- and post-contrast GE signals at the 10 ms and 40 ms. The same equations were applied to compute  $\Delta R_2$  from the SE signal at 120 ms. The mean  $\pm$ SD of the VSI values for the test VOIs and their MRE with the true mean radius are also reported.

For visual demonstration of our method, maps of true and predicted CBV were generated, along with maps of CV and BC for the true and predicted VSDs, at a resolution equivalent to LSFM, across a stack of 123 axial slices of segmented mouse brain vasculature. The maps of true and predicted mean radius and VSI values over the same stack was also computed. To achieve this, the stack was divided into non-overlapping VOIs, each with an array size of  $123 \times 123 \times 123$ . The true parameter values were computed using LSFM-based algorithms, while the trained model was used to predict the corresponding parameters for each VOI. The computed values were then assigned back to all non-zero voxels within the corresponding VOIs in the binary LSFM vasculature stack, preserving spatial resolution. Finally, parameter maps for the entire stack were assembled by stitching together the corresponding VOI-based maps. The MAD between the true and predicted maps for each parameter are reported.

The DL models were also tested on a publicly available dataset containing VOIs of segmented vasculature from a mouse brain.<sup>29</sup> 1,000 VOIs were randomly selected and resampled to 1.8  $\mu\text{m}$  isotropic resolution and cropped to the array size of  $123 \times 123 \times 123$ . The simulated GESFIDE signal from each VOI was passed through the trained CBVE and VSDE models to predict the CBV and VSD, respectively. The mean  $\pm$  SD of the true and predicted CBV, mean vessel radius, and CV were computed. The Pearson

correlation ( $r$ ) and MRE between true and predicted CBV were computed. The mean $\pm$ SD of BC values between the true and predicted VSDs was computed and the MRE between the true and predicted mean vessel radius were measured. The mean $\pm$ SD of the VSI values for the VOIs and their MRE with the true mean radius are also reported.

## Data Availability

---

While the full dataset cannot be shared due to its large size (~1TB), sample data will be provided.

The complete raw and segmented LSFM images will be available upon reasonable request.

## Code Availability

---

The source code and sample test data used in this paper is available online at [https://github.mdanderson.org/NeuroCare/VSD\\_Pipeline.git](https://github.mdanderson.org/NeuroCare/VSD_Pipeline.git).

## References

---

- [1] P Carmeliet and RK Jain, "Angiogenesis in cancer and other diseases," *Nature*, **407**, 249-57, 2000.
- [2] RA Gatenby and RJ Gillies, "A microenvironmental model of carcinogenesis," *Nat Rev Cancer*, **8**, 56-61, 2008.
- [3] D Hanahan and RA Weinberg, "Hallmarks of cancer: the next generation," *Cell*, **144**, 646-74, 2011.
- [4] JA Nagy, AM Dvorak, and HF Dvorak, "Vascular hyperpermeability, angiogenesis, and stroma generation," *Cold Spring Harb Perspect Med*, **2**, a006544, 2012, PubMed Central PMCID: PMC3281587.
- [5] R Ross, "Atherosclerosis--an inflammatory disease," *N Engl J Med*, **340**, 115-26, 1999.
- [6] R Bataller and DA Brenner, "Liver fibrosis," *J Clin Invest*, **115**, 209-18, 2005, PubMed Central PMCID: PMC3281587.
- [7] Z Temurer Afsar, B Aycicek, Y Tutuncu, U Cavdar, and E Sennaroglu, "Relationships between microvascular complications of diabetes mellitus and levels of macro and trace elements," *Minerva Endocrinol (Torino)*, **48**, 305-310, 2023.
- [8] L Ostergaard, TS Engedal, F Moreton, MB Hansen, JM Wardlaw, T Dalkara, HS Markus, and KW Muir, "Cerebral small vessel disease: Capillary pathways to stroke and cognitive decline," *J Cereb Blood Flow Metab*, **36**, 302-25, 2016, PubMed Central PMCID: PMC3281587.
- [9] L Pantoni, "Cerebral small vessel disease: from pathogenesis and clinical characteristics to therapeutic challenges," *The Lancet Neurology*, **9**, 689-701, 2010.
- [10] C Iadecola, "Neurovascular regulation in the normal brain and in Alzheimer's disease," *Nat Rev Neurosci*, **5**, 347-60, 2004.

- [11] BV Zlokovic, "Neurovascular pathways to neurodegeneration in Alzheimer's disease and other disorders," *Nat Rev Neurosci*, **12**, 723-38, 2011, PubMed Central PMCID: PMCPMC4036520.
- [12] G Paul and OF Elabi, "Microvascular Changes in Parkinson's Disease- Focus on the Neurovascular Unit," *Front Aging Neurosci*, **14**, 853372, 2022, PubMed Central PMCID: PMCPMC8960855.
- [13] MD Sweeney, AP Sagare, and BV Zlokovic, "Blood-brain barrier breakdown in Alzheimer disease and other neurodegenerative disorders," *Nat Rev Neurol*, **14**, 133-150, 2018, PubMed Central PMCID: PMCPMC5829048.
- [14] L Ostergaard, RM Weisskoff, DA Chesler, C Gyldensted, and BR Rosen, "High resolution measurement of cerebral blood flow using intravascular tracer bolus passages. Part I: Mathematical approach and statistical analysis," *Magn Reson Med*, **36**, 715-25, 1996.
- [15] I Tropres, S Grimault, A Vaeth, E Grillon, C Julien, JF Payen, L Lamalle, and M Décorps, "Vessel size imaging," *Magnetic Resonance in Medicine*, **45**, 397-408, 2001.
- [16] M Beaumont, B Lemasson, R Farion, C Segebarth, C Remy, and EL Barbier, "Characterization of tumor angiogenesis in rat brain using iron-based vessel size index MRI in combination with gadolinium-based dynamic contrast-enhanced MRI," *J Cereb Blood Flow Metab*, **29**, 1714-26, 2009, PubMed Central PMCID: PMCPMC3348120.
- [17] KM Donahue, HG Krouwer, SD Rand, AP Pathak, CS Marszalkowski, SC Censky, and RW Prost, "Utility of simultaneously acquired gradient-echo and spin-echo cerebral blood volume and morphology maps in brain tumor patients," *Magn Reson Med*, **43**, 845-53, 2000.
- [18] N Pannetier, B Lemasson, T Christen, M Tachrount, I Tropres, R Farion, C Segebarth, C Remy, and EL Barbier, "Vessel size index measurements in a rat model of glioma: comparison of the dynamic (Gd) and steady-state (iron-oxide) susceptibility contrast MRI approaches," *NMR Biomed*, **25**, 218-26, 2012.
- [19] CC Quarles and KM Schmainda, "Assessment of the morphological and functional effects of the anti-angiogenic agent SU11657 on 9L gliosarcoma vasculature using dynamic susceptibility contrast MRI," *Magn Reson Med*, **57**, 680-7, 2007.
- [20] LA Stables, RP Kennan, and JC Gore, "Asymmetric spin-echo imaging of magnetically inhomogeneous systems: theory, experiment, and numerical studies," *Magn Reson Med*, **40**, 432-42, 1998.
- [21] JL Boxerman, LM Hamberg, BR Rosen, and RM Weisskoff, "MR contrast due to intravascular magnetic susceptibility perturbations," *Magn Reson Med*, **34**, 555-66, 1995.
- [22] J Dennie, JB Mandeville, JL Boxerman, SD Packard, BR Rosen, and RM Weisskoff, "NMR imaging of changes in vascular morphology due to tumor angiogenesis," *Magnetic Resonance in Medicine*, **40**, 793-799, 1998.
- [23] J Jensen and R Chandra, "MR imaging of microvasculature," *Magnetic Resonance in Medicine*, **44**, 224-230, 2000.
- [24] V Kiselev and S Posse, "Analytical model of susceptibility - induced MR signal dephasing: effect of diffusion in a microvascular network," *Magnetic Resonance in Medicine*, **41**, 499-509, 1999.
- [25] F Boux, F Forbes, J Arbel, B Lemasson, and EL Barbier, "Bayesian inverse regression for vascular magnetic resonance fingerprinting," *IEEE Transactions on Medical Imaging*, **40**, 1827-1837, 2021.

- [26] T Christen, N Pannetier, WW Ni, D Qiu, ME Moseley, N Schuff, and G Zaharchuk, "MR vascular fingerprinting: A new approach to compute cerebral blood volume, mean vessel radius, and oxygenation maps in the human brain," *NeuroImage*, **89**, 262-270, 2014.
- [27] A Delphin, F Boux, C Brossard, T Coudert, JM Warnking, B Lemasson, EL Barbier, and T Christen, "Enhancing MR vascular Fingerprinting with realistic microvascular geometries," *Imaging Neuroscience*, **2**, 1-13, 2024.
- [28] P Pouliot, L Gagnon, T Lam, PK Avti, C Bowen, M Desjardins, AK Kakkar, E Thorin, S Sakadzic, and DA Boas, "Magnetic resonance fingerprinting based on realistic vasculature in mice," *NeuroImage*, **149**, 436-445, 2017.
- [29] MI Todorov, JC Paetzold, O Schoppe, G Tetteh, V Efremov, K Völgyi, M Düring, M Dichgans, M Piraud, and B Menze, "Automated analysis of whole brain vasculature using machine learning," *BioRxiv*, 613257, 2019.
- [30] AP Pathak, KM Schmainda, BD Ward, J Linderman, KJ Rebro, and AS Greene, "MR - derived cerebral blood volume maps: issues regarding histological validation and assessment of tumor angiogenesis," *Magnetic Resonance in Medicine: An Official Journal of the International Society for Magnetic Resonance in Medicine*, **46**, 735-747, 2001.
- [31] A Chakhoyan, J Yao, K Leu, WB Pope, N Salamon, W Yong, A Lai, PL Nghiemphu, RG Everson, and RM Prins, "Validation of vessel size imaging (VSI) in high-grade human gliomas using magnetic resonance imaging, image-guided biopsies, and quantitative immunohistochemistry," *Scientific Reports*, **9**, 2846, 2019.
- [32] R Jain, J Gutierrez, J Narang, L Scarpace, L Schultz, N Lemke, S Patel, T Mikkelsen, and J Rock, "In vivo correlation of tumor blood volume and permeability with histologic and molecular angiogenic markers in gliomas," *American Journal of Neuroradiology*, **32**, 388-394, 2011.
- [33] LC Bell, MD Does, AM Stokes, LC Baxter, KM Schmainda, AC Dueck, and CC Quarles, "Optimization of DSC MRI echo times for CBV measurements using error analysis in a pilot study of high-grade gliomas," *American Journal of Neuroradiology*, **38**, 1710-1715, 2017.
- [34] E Kellner, T Breyer, P Gall, K Müller, M Trippel, O Staszewski, F Stein, O Saborowski, O Dyakova, and H Urbach, "MR evaluation of vessel size imaging of human gliomas: Validation by histopathology," *Journal of Magnetic Resonance Imaging*, **42**, 1117-1125, 2015.
- [35] I Tropès, N Pannetier, S Grand, B Lemasson, A Moisan, M Péoc'h, C Rémy, and EL Barbier, "Imaging the microvessel caliber and density: principles and applications of microvascular MRI," *Magnetic Resonance in Medicine*, **73**, 325-341, 2015.
- [36] DA Yablonskiy and EM Haacke, "Theory of NMR signal behavior in magnetically inhomogeneous tissues: the static dephasing regime," *Magnetic Resonance in Medicine*, **32**, 749-763, 1994.
- [37] ML Scarpelli, DR Healey, S Mehta, VD Kodibagkar, and CC Quarles, "A practical method for multimodal registration and assessment of whole-brain disease burden using PET, MRI, and optical imaging," *Scientific Reports*, **10**, 17324, 2020.
- [38] Y-G Park, CH Sohn, R Chen, M McCue, DH Yun, GT Drummond, T Ku, NB Evans, HC Oak, and W Trieu, "Protection of tissue physicochemical properties using polyfunctional crosslinkers," *Nature biotechnology*, **37**, 73-83, 2019.
- [39] CH Li and C Lee, "Minimum cross entropy thresholding," *Pattern Recognition*, **26**, 617-625, 1993.

- [40] T-C Lee, RL Kashyap, and C-N Chu, "Building skeleton models via 3-D medial surface axis thinning algorithms," *CVGIP: Graphical Models and Image Processing*, **56**, 462-478, 1994.
- [41] Y Liu, D Jin, C Li, KF Janz, TL Burns, JC Torner, SM Levy, and PK Saha, "A robust algorithm for thickness computation at low resolution and its application to in vivo trabecular bone CT imaging," *IEEE Transactions on Biomedical Engineering*, **61**, 2057-2069, 2014, PubMed Central PMCID: PMCNIHMSID696943.
- [42] NB Semmineh, AM Stokes, LC Bell, JL Boxerman, and CC Quarles, "A Population-Based Digital Reference Object (DRO) for Optimizing Dynamic Susceptibility Contrast (DSC)-MRI Methods for Clinical Trials," *Tomography*, **3**, 41-49, 2017, PubMed Central PMCID: PMCPMC5454781.
- [43] NB Semmineh, J Xu, JL Boxerman, GW Delaney, PW Cleary, JC Gore, and CC Quarles, "An efficient computational approach to characterize DSC-MRI signals arising from three-dimensional heterogeneous tissue structures," *PLoS One*, **9**, e84764, 2014, PubMed Central PMCID: PMCPMC3885618.
- [44] K Fukushima, "Visual feature extraction by a multilayered network of analog threshold elements," *IEEE Transactions on Systems Science and Cybernetics*, **5**, 322-333, 1969.
- [45] J Han and C Moraga, "The influence of the sigmoid function parameters on the speed of backpropagation learning," Proc. of *International Workshop on Artificial Neural Networks*, 195-201, 1995.
- [46] K He, X Zhang, S Ren, and J Sun, "Delving deep into rectifiers: Surpassing human-level performance on imagenet classification," Proc. of *Proceedings of the IEEE International Conference on Computer Vision*, 1026-1034, 2015.
- [47] DP Kingma and J Ba, "Adam: A method for stochastic optimization," *arXiv preprint arXiv:1412.6980*, 2014.
- [48] AM Stokes and CC Quarles, "A simplified spin and gradient echo approach for brain tumor perfusion imaging," *Magnetic Resonance in Medicine*, **75**, 356-362, 2016.

## **Acknowledgements (optional)**

---

This work was supported by Cancer Prevention and Research Institute of Texas (CPRIT) RR220038 (C. Chad Quarles is a CPRIT scholar in cancer research), MD Anderson's Advanced Technology Genomics Core (supported by NIH 1S10OD024977-01 and NCI P30CA0166722), Research Histology Core Laboratory (supported by NCI P30CA0166722), Advanced Microscopy Core (supported by NIH S10RR029552), and Advanced Cytometry & Sorting Facility (supported by NCI P30CA0166722).

## **Ethics declarations**

---

The authors have no competing interests.

## Figures

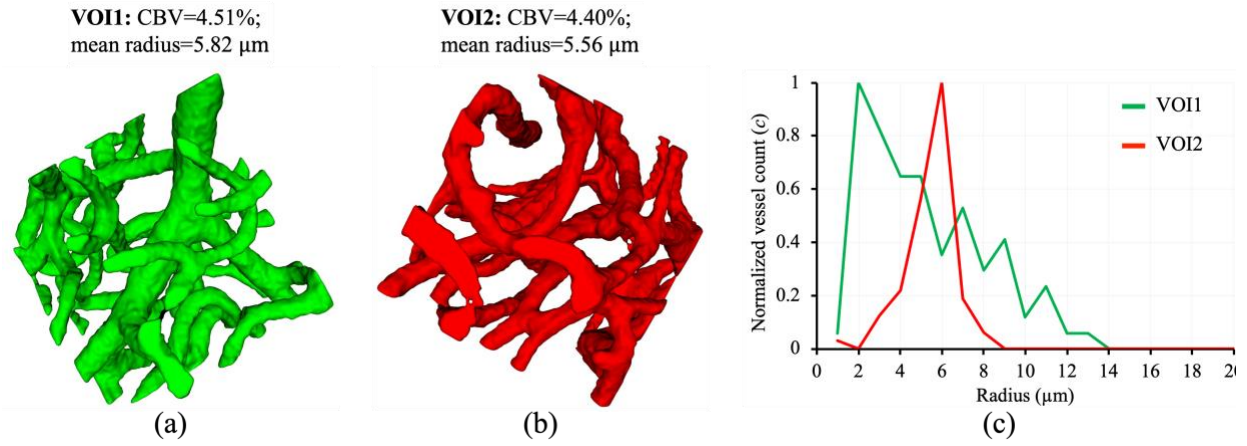


Fig. 1. Two representative VOIs (a,b) extracted from LSFM image of a mouse-brain vasculature with similar CBV and mean radius but different VSDs (c).

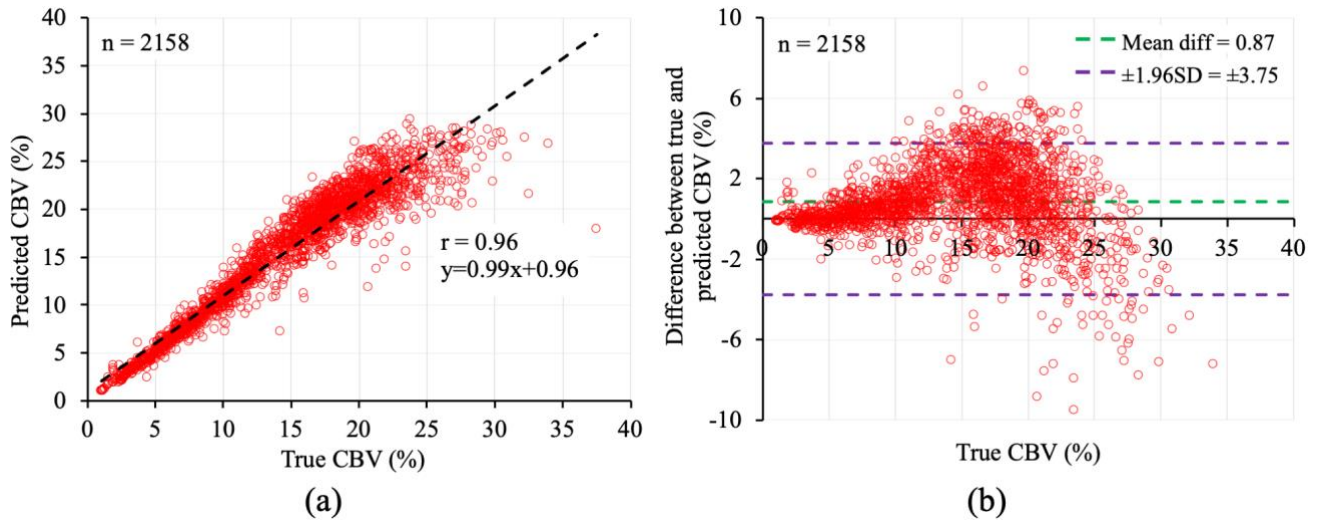


Fig. 2. The Pearson correlation (a) and Bland-Altman plot (b) of true and predicted CBV (n=2,158).

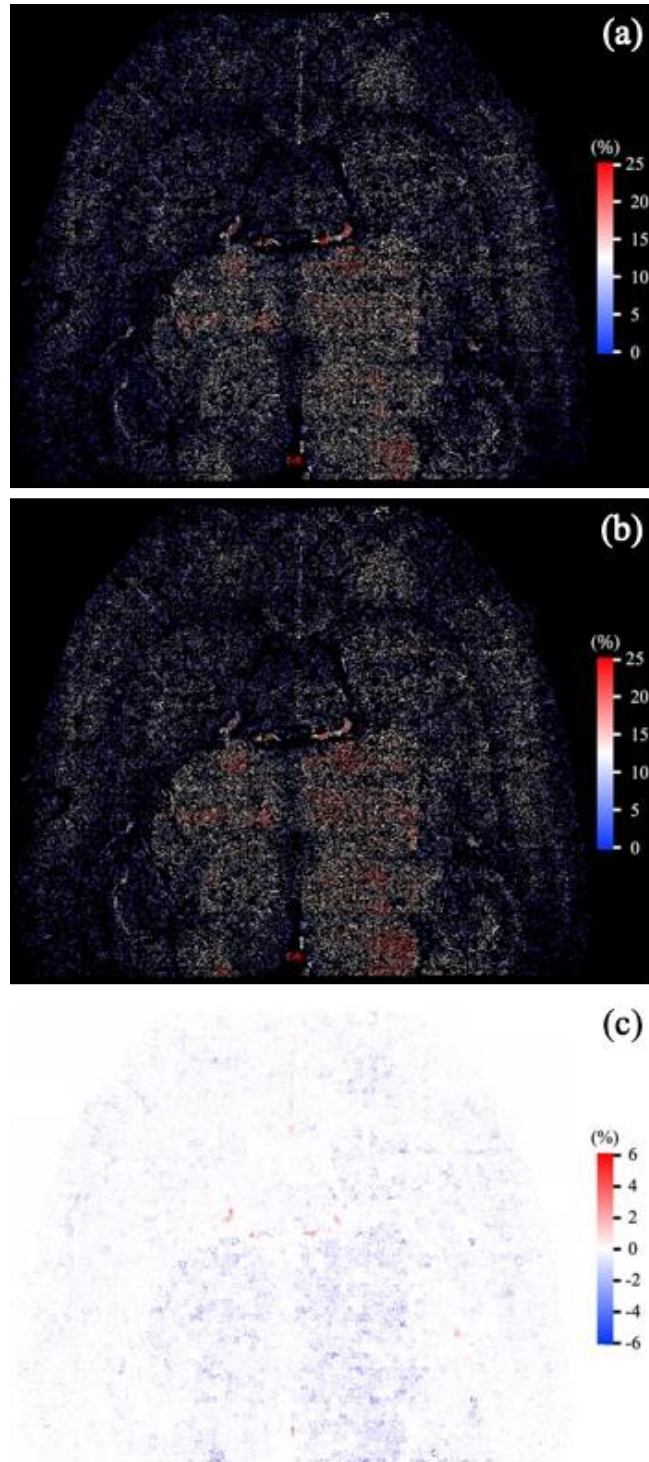


Fig. 3. Color-coded maps of true (a) and predicted (b) CBV values over an entire axial slice of mouse whole brain LSFM image. The residual map of the true and predicted CBV values is shown in (c).

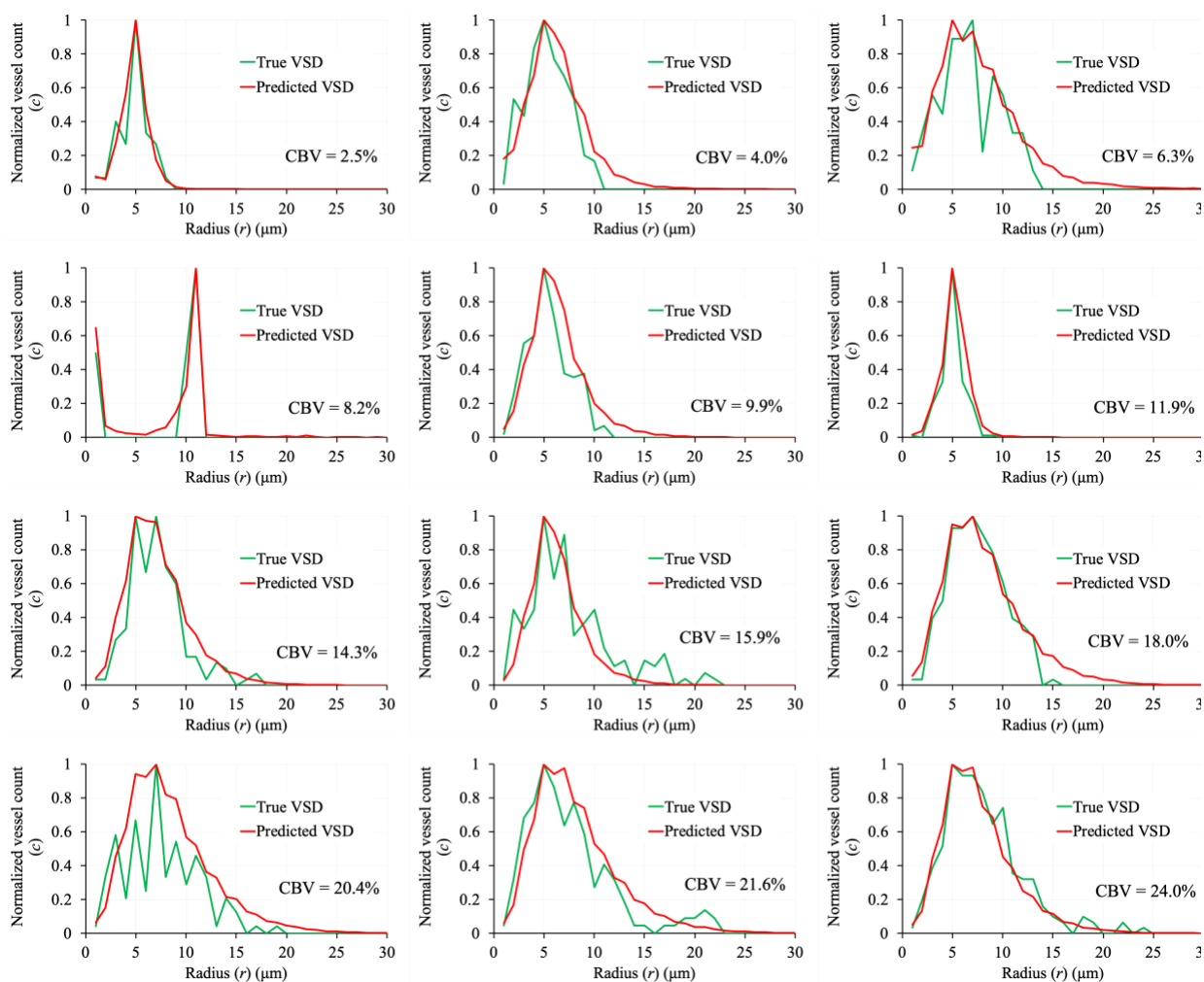


Fig. 4. The true (green) and predicted (red) VSDs for 12 VOIs with CBV varying from 2.5 to 24%. Significant overlap between the true and predicted VSDs are noticeable despite the true VSD being noisy and of varying shape.

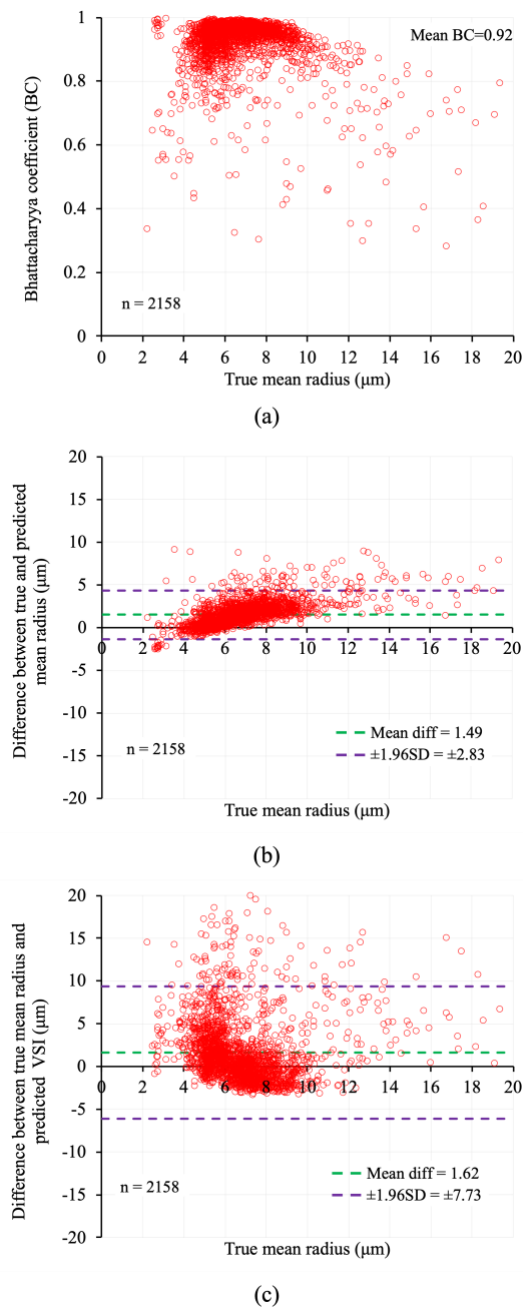


Fig. 5. The results of quantitative evaluation for the VSDE. (a) Distribution of the BC values against the true mean radius for the test VOIs ( $n=2,158$ ). (b) The Bland-Altman plot of difference between true and predicted mean radius. (c) Same as (b) but for the difference between true mean radius and VSI.

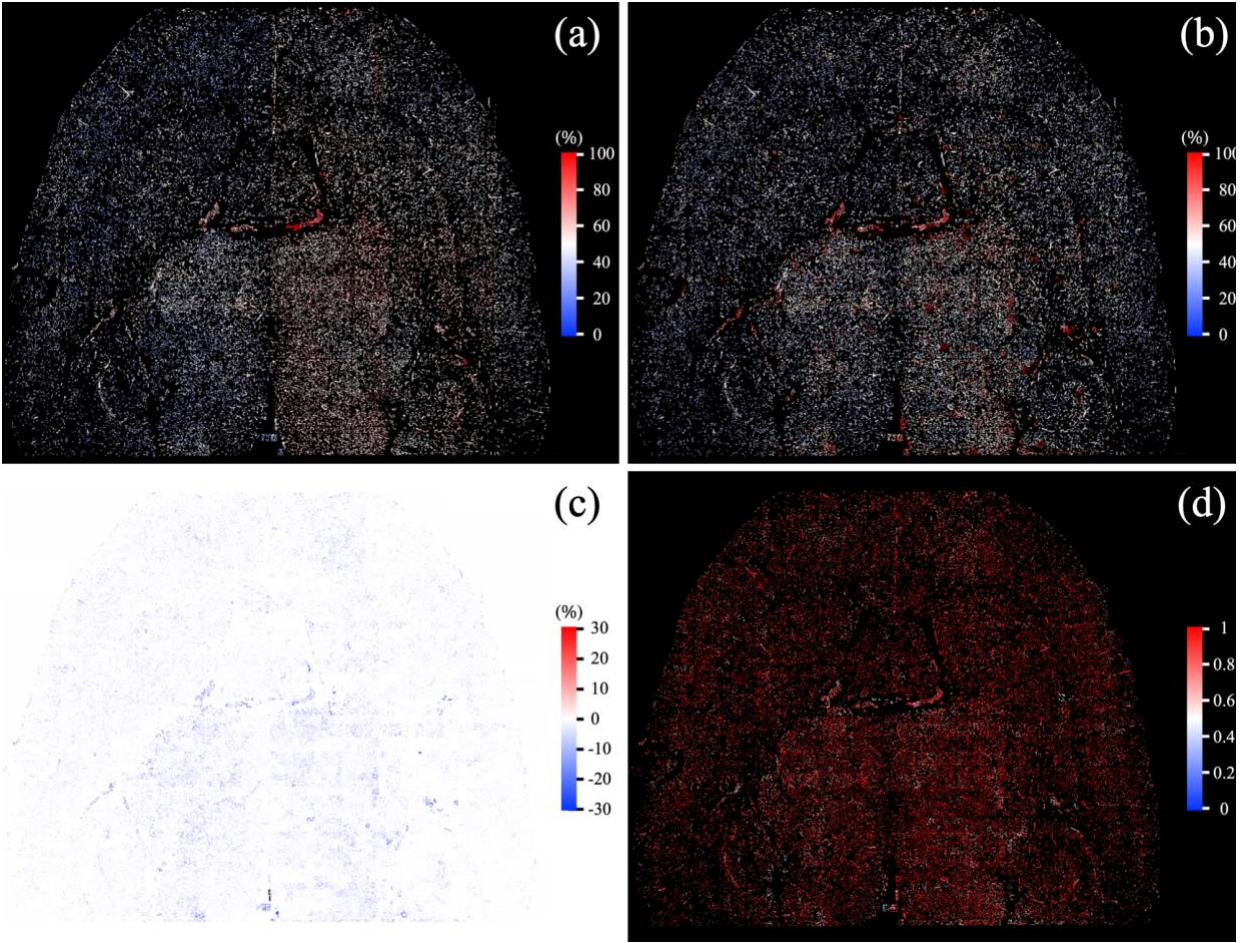


Fig. 6. Qualitative results of VSD prediction on an entire axial slice of mouse whole brain LSFM image.

(a,b) Color-coded coefficient of variance (CV) maps of the true (a) and predicted (b) VSDs. (c) The residual map of the true and predicted CV maps. (d) The map of BC values measured between the true and predicted VSDs.

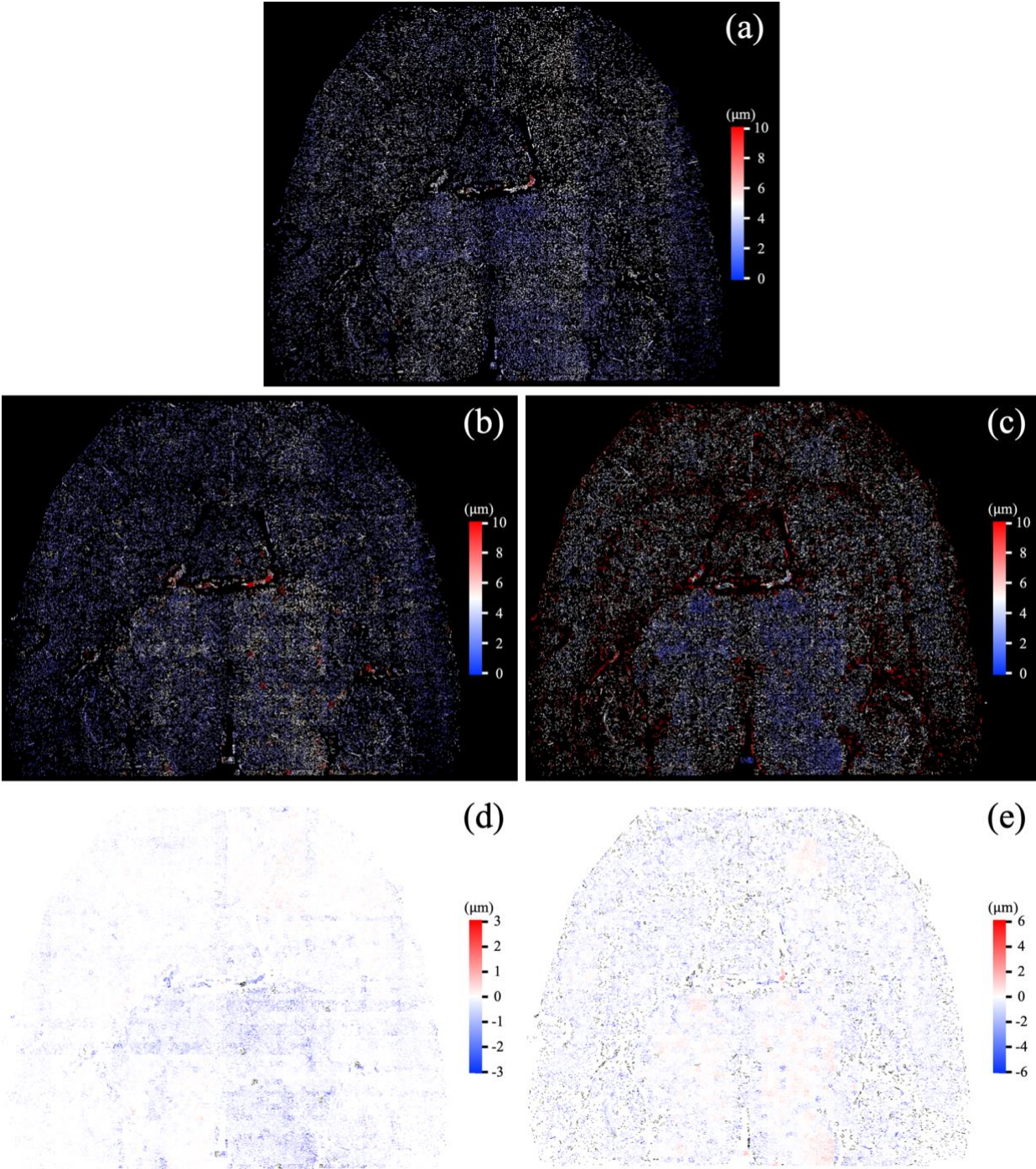


Fig. 7. Qualitative results of mean vessel radius and VSI computation on an entire axial slice of mouse whole brain LSFM image. (a-c) Color-coded maps of the true (a) and predicted (b) mean radius and VSI (c) values. (d,e) The residual map of true and predicted mean radius and the true mean radius and VSI.

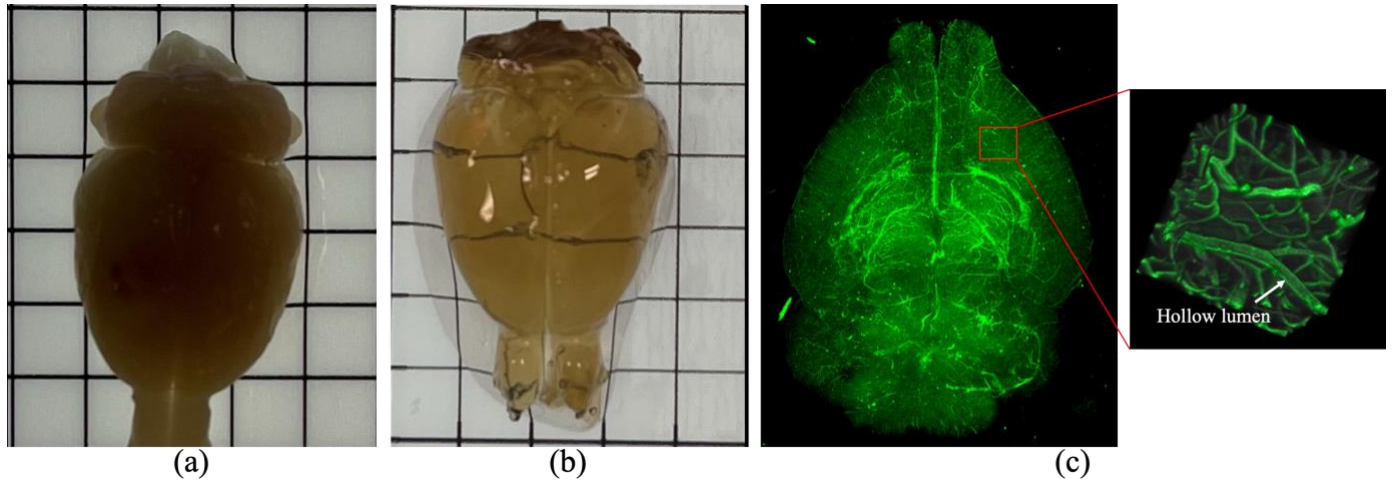


Fig. 8. Steps involved in animal preparation and LSFM imaging of a rat brain. (a) A rat brain after skull removal. (b) Same brain after tissue clearing. (c) Three-dimensional (3D) rendition of an entire rat brain vasculature along with a zoomed in volume of interest (VOI) for better representation of the highlighted vessels. Note that, large vessels have hollow lumen (white arrow) as lectin only stains the vessel walls. This approach enables the visualization of blood vessels down to capillary size.

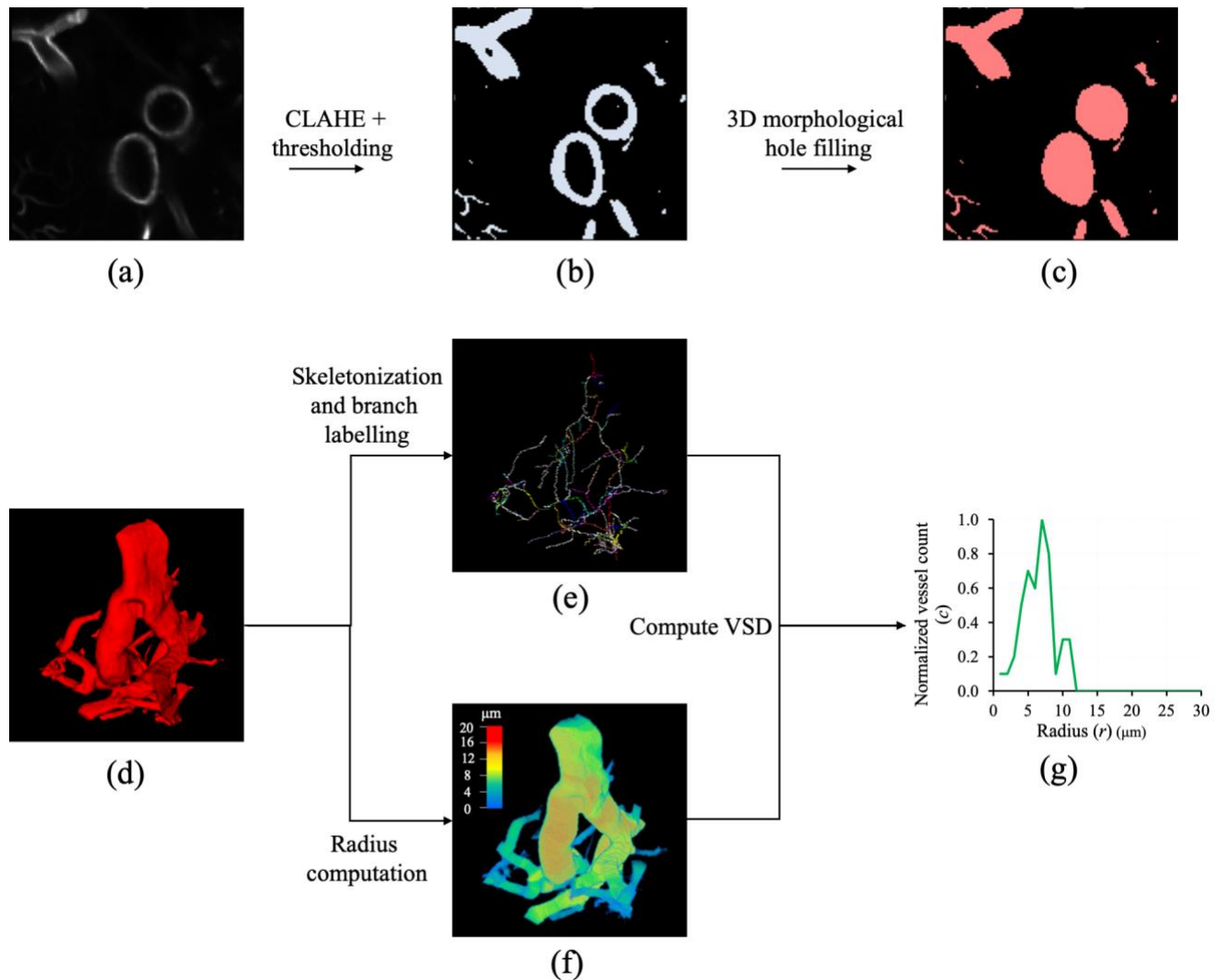


Fig. 9. Steps involved in binary segmentation of the vasculature from a LSFM image and computation of the VSD. (a) Axial view of a LSFM VOI with an array size of  $123 \times 123 \times 123$ . (b) Segmented vasculature from (a) after contrast limited adaptive histogram equalization (CLAHE) and binary thresholding<sup>39</sup>. (c) Same as (b) but after applying morphological hole filling to close the hollow lumen of the large vessels. (d) 3D rendition of the maximally connected segmented vascular network. (e) Skeleton of (d) where individual vessels are uniquely labelled by distinct colours. (f) Color-coded rendition of voxel-wise radius map of (d). (g) True VSD of (d) computed as the normalized histogram of vessel radius values with a bin size of  $1 \mu\text{m}$ . See text for details.

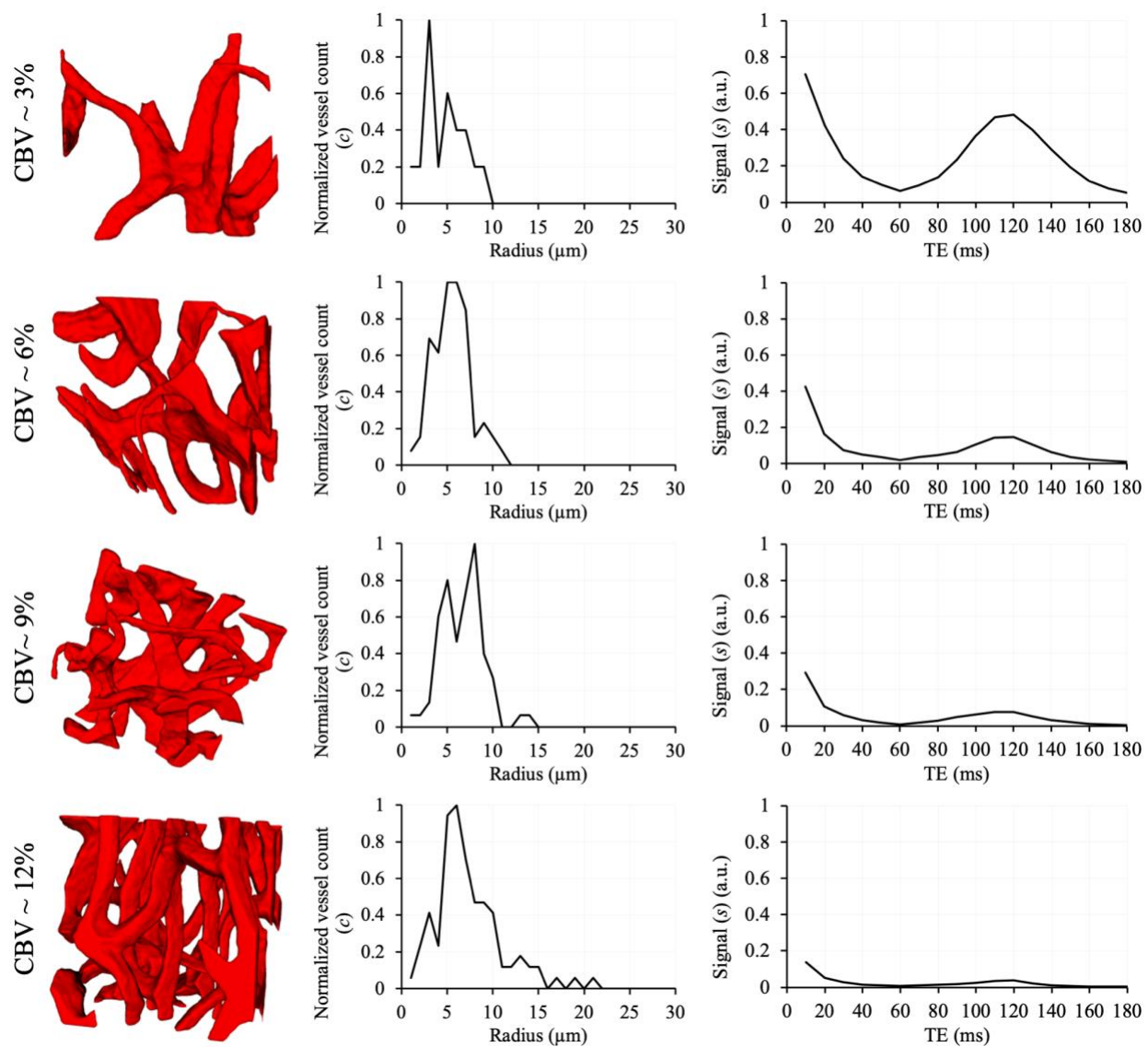


Fig. 10. Example VOIs (1st column) extracted from LSFM images with varying CBV and the corresponding VSD (2nd column) and ratio of simulated pre- and post-contrast GESFIDE signals (3rd column). Variations in signal at a specific echo time result from disparities in vessel size, orientation, and CBV.

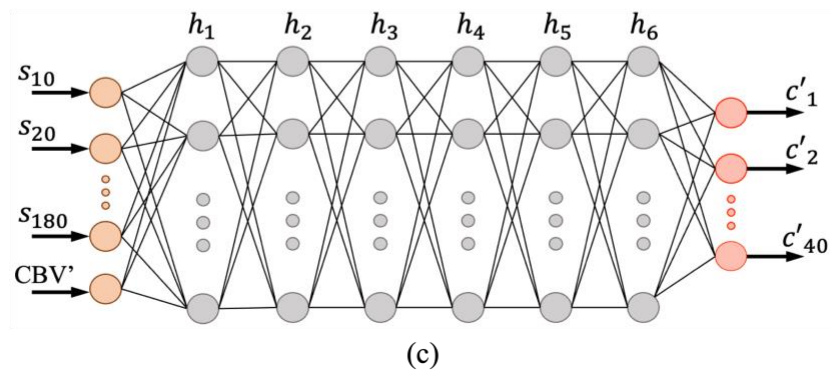
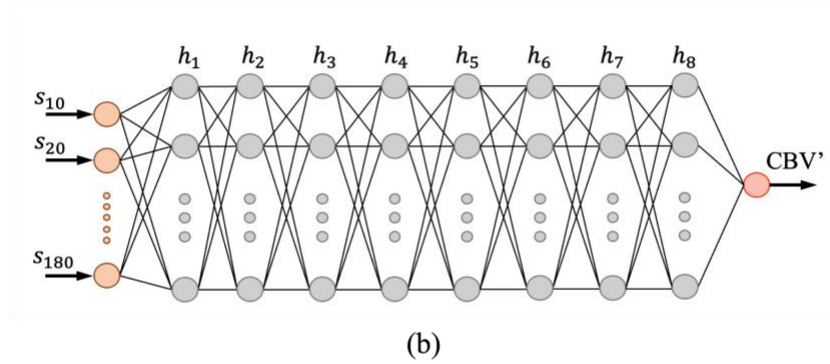
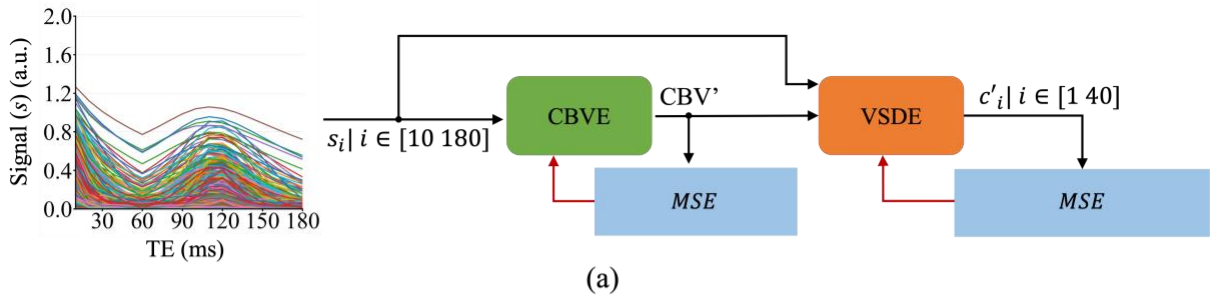


Fig. 11. The DL framework used to predict the VSD from a given GESFIDE signal. (a) Two FCNs called the CBVE and VSDE are trained simultaneously to predict the CBV and the VSD from the GESFIDE signal, respectively. (b,c) The network architecture of the CBVE (b) and VSDE (c); see text for details.